JOURNAL OF THERMOPHYSICS AND HEAT TRANSFER
Vol. 12, No. 4, October–December 1998

Gas Permeability of Rigid Fibrous Refractory Insulations

Jochen Marschall* and Frank S. Milos†
NASA Ames Research Center, Moffett Field, California 94035-1000

An experimental procedure is developed for measuring the gas permeability of rigid fibrous tile insulations. Permeability data are documented for a variety of ceramic fiber insulations from the LI, AIM, FRCI, and AETB families, as well as for the commercial carbon fiber insulation FiberForm®. It is demonstrated that rarefied-flow effects are significant for gas flow through such materials and that the pressure dependence of gas permeability is well represented by the Klinkenberg formulation. Continuum permeabilities ranging from 3 to 63 × 10^{-12} m^2 are found for all materials except FiberForm, which has a significantly higher continuum permeability on the order of 10^{-10} m^2. The room temperature permeability slip parameter for air is found to range from 603 to 7940 Pa. A scaling relation that allows calculation of permeability slip parameters for other gases and for varying temperature is validated by experiment. The dependency of the permeability on material density, anisotropic microstructure, and constituent fiber size is presented. To illustrate an application of this permeability data, representative computations for the gas flow through a rigid fibrous vent of a space probe during launch and atmospheric entry are given.

Nomenclature

A = plug or vent area, m^2
A' = effective heat transfer area, m^2
b = permeability slip parameter, Pa
C_p = heat capacity, J/kg-K
D = sample diameter, m
d = capillary diameter, m
F = measurable quantity in Eq. (7), N
H = effective heat transfer coefficient, W/m^2-K
h = enthalpy, J/kg
K = effective permeability, m^2
Kn = Knudsen number
K_0 = continuum flow permeability, m^2
L = length, m
M = molar mass, kg/mol
m = mass, kg
$\dot{m}$ = mass flow rate, kg/s
P = pressure, Pa
P_{av} = average pressure $(P_1 + P_2)/2$, Pa
q = heat flux, W/m^2
R = universal gas constant, J/mol K
Re = Reynolds number
T = temperature, K
t = time, s
u = internal energy, J/kg
V = volume, m^3
ΔP = pressure difference $P_1 - P_2$, Pa
ε = emittance
μ = viscosity, N s/m^2
σ = Stefan–Boltzmann constant, W/m^2-K^4
ρ = density, kg/m^3

Subscripts
ext = external
g = gas
H = hole
int = internal
P = plug or vent
ref = reference
s = solid
1 = upstream
2 = downstream

Introduction

RIGID fibrous refractory insulations are integral components of the thermal protection system (TPS) of many hypersonic vehicles and spacecraft. These low-density materials have open, highly porous microstructures consisting of interlaced refractory fibers that typically take up less than 20% of the bulk insulation volume. This open porosity makes TPS tile materials permeable to gas flow. There are numerous instances in which internal gas transport in a thermal protection system can be important; examples include the penetration of hot boundary-layer gases, the flow of decomposition (pyrolysis) products, and the use of convective flows to mitigate ice formation caused by cryopumping.

The gas permeability of a porous material must be known before the gas flow through it can be modeled; however, this property has not previously been available for the rigid fibrous insulations used in many thermal protection systems. This paper presents an experimental procedure to measure the gas permeability of such fibrous insulations[1] and documents permeability data that were obtained for a variety of ceramic fiber insulations from the LI, AIM, FRCI, and AETB families, as well as the commercial carbon fiber product FiberForm®. These families of ceramic fiber insulations were developed as reusable TPS materials that combine a high-temperature capability with good thermal insulative properties and a measure of mechanical strength, while minimizing weight.[2–4] LI, FRCI, and AETB insulations are currently used on the Space Shuttle Orbiter. It is demonstrated here that rarefied-flow effects are significant in such materials and that the pressure dependence of the permeability is well represented by the Klinkenberg[5] formulation. This formulation contains a material specific constant (the continuum permeability) and a temperature and gas-dependent parameter (the permeability slip parameter). A scal-

Received Jan. 2, 1998; revision received May 7, 1998; accepted for publication May 11, 1998.

*Senior Research Scientist, Thermosciences Institute, Eloret Corporation. E-mail: jmarschall@mail.arc.nasa.gov. Member AIAA.

†Aerospace Engineer, Thermal Protection Materials and Systems Branch. E-mail: fmilos@mail.arc.nasa.gov. Senior Member AIAA.

ing relation, which allows for the calculation of permeability slip parameters for gases other than air and for varying temperatures, is presented and validated by experiment. The directional anisotropy of permeability and the dependence of permeability on material density and fiber size are also presented. Finally, the representative computations of gas flow through a rigid fibrous material are given to illustrate potential applications of the permeability data presented herein.

Materials

LI, AIM, FRCI, and AETB insulations[2-4] are composed of ceramic fibers with diameters on the order of 1–8 μm. They are made by combining constituent fibers into a water-based slurry, axially compressing the slurry in a casting tower, removing moisture from the pressed billet in a drying oven, and then firing the billet in a high-temperature furnace. The resulting fiber structure is three dimensional and highly complex, yet also markedly anisotropic because the fibers preferentially align normal to the pressing direction. An analogous process is used to make the carbon fiber insulation FiberForm, with a similar microstructural result. Owing to this microstructural anisotropy, the material properties are in general orthotropic.

As illustrated in Fig. 1, the pressing axis is defined herein as the "transverse" direction, whereas directions normal to the pressing axis are termed "in-plane." (The transverse direction is also called the "through thickness" direction in the literature.) Fibers are aligned preferentially along in-plane directions. The gas permeability of materials was determined for both orthogonal directions by cutting test specimens with orientations as shown in Fig. 1 from billets of the bulk material.

The TPS materials tested were LI-900, LI-2200, AIM-18, FRCI-12, AETB-12, and FiberForm. LI-900, LI-2200, and AIM-18 tiles are composed of silica fibers, FRCI-12 tiles contain 80 wt% silica and 20 wt% Nextel® (aluminoborosilicate fibers manufactured by 3M), and AETB-12 tiles consist of 68 wt% silica, 20 wt% alumina, and 12 wt% Nextel. All of these insulations, except for LI-900, also contain less than 2 wt% of SiC particulate that acts as an emittance enhancement agent. The nominal tile densities[2-4] are 144 kg/m^3 (9 lb/ft^3) for LI-900, 352 kg/m^3 (22 lb/ft^3) for LI-2200, 288 kg/m^3 (18 lb/ft^3) for AIM-18, and 192 kg/m^3 (12 lb/ft^3) for FRCI-12 and AETB-12. FiberForm is a commercially available carbon-fiber tile manufactured by Fiber Materials, Inc., which has a density ranging from about 152 to 176 kg/m^3 (9.5 to 11 lb/ft^3). Because subtle processing deviations can cause inter- and intrabillet density variations, a specimen machined from bulk material can have a density significantly different from the nominal value. Density variations within a given test specimen are minimal.

Experiment

The experimental setup used to determine room temperature permeability is illustrated in Fig. 2. Cylindrical specimens were placed within a brass test section that was connected to a mechanical vacuum pump on one side and to a gas inlet line on the other. Three interchangeable test sections were available to accept samples with diameters of 2.54 cm, 1.796 cm, or 1.27 cm. The test sections were comprised of two parts, the longer of which could house specimens up to 8 cm in length. The inside surfaces of the test sections were precision bored to obtain the smoothest finish possible. Test specimens were turned on a lathe to diameters several thousandth of an inch (25–50 μm) oversize and were press-fit into the test section to mitigate against gas leakage along the sides. Because rigid fibrous insulations are friable, specimens were not reused. Additionally, the interface between the sample and test section was overlapped on the downstream side by a silicone-rubber gasket that protruded about 0.02 cm into the bore of the test chamber. This gasket also served to seal the bolted flange connection between the two parts of the test section. The standard dimensions of the samples tested in this study were 1.27 cm

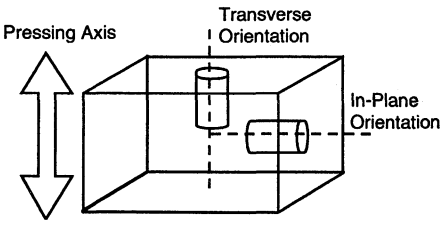

Fig. 1 Orientation of the test specimens relative to tile billet.

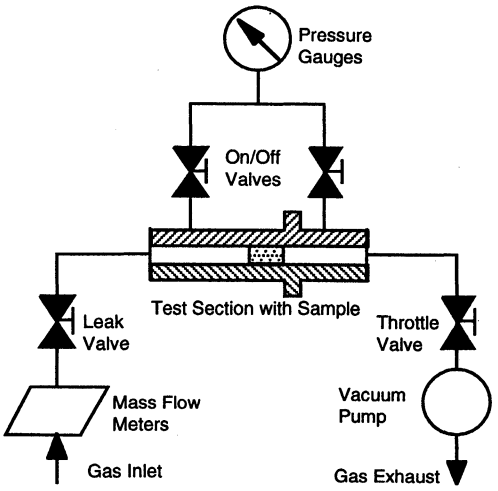

Fig. 2 Experimental apparatus used to determine gas permeability.

in diameter and 2 cm in length, with the exception of the AIM-18 specimens, which were 2.54 cm in diameter and 3.43 cm in length.

Baratron-type capacitance manometer gauges (133 and 13.3 kPa ranges) were used to measure the gas pressures upstream and downstream of the sample. A manifold with several on/off valves allowed the same pressure gauge to read both upstream and downstream pressures in succession. Gases were introduced via a variable leak valve, and the flow rate was monitored using calibrated Tylan flow meters (ranges of 30, 300, 1000, and 5000 SCCM). Various combinations of pressure and flow rate were achieved by adjustments of the leak valve and the throttling valve in the vacuum line. Measurements were made using the combination of pressure gauge and flow meter with the best operating range for each experimental condition. Three type-K thermocouples were used, together with a Stanford Research Systems thermocouple monitor, to measure the ambient room temperature, the temperature of the inlet line, and the temperature of the brass test section. All measurements using this experimental setup were made in the temperature range of 285–300 K and the pressure range of 0.5–70 kPa. Tests proceeded by adjusting the throttle and leak valves to obtain various combinations of downstream pressure and gas flow rate while maintaining a fixed upstream pressure. This procedure was repeated at various upstream pressures to canvas the entire pressure range of interest. The test gas was room air, except for one test conducted with helium to confirm the dependence of permeability on gas composition.

An additional experiment was conducted to validate the temperature dependence of permeability. The general experimental layout was similar to that shown in Fig. 2; however, the test section was made of a 2.2 cm i.d. quartz tube that was enclosed by a three-zone Lindberg electric tube furnace. A 3-cm-long test specimen was machined to give a tight press-fit into the quartz tube. The furnace hot zone was 45.7 cm long, and the sample was positioned slightly off center in the furnace to ensure temperature equilibration between the in-flowing gas and the sample. The heated length of quartz tube upstream of

the sample was sufficient to produce fully developed thermal conditions in a laminar flow, with minimal (less than 5 K) radial temperature variations in the gas, according to relations presented in Ref. 6. The sample and gas temperatures were thus assumed equivalent to the furnace temperature that was measured with three type K thermocouples, one in each zone. Gas pressures and flow rates were monitored with the same instrumentation described earlier. Pure nitrogen was used as the test gas.

Data Analysis

Axial gas flow through a cylindrical porous test specimen can be described by combining the ideal gas law, conservation of mass, and the differential form of Darcy's law, to yield the relation

$$\dot{m} = -\frac{\pi D^2 M}{4\mu RT} KP \frac{dP}{dx} \tag{1}$$

Aside from the permeability and geometric factors, this equation has the same form as the well-known Hagen–Poiseuille relation for viscous gas flow ($Kn << 1$) in a straight capillary tube.[5,7] If the characteristic pore dimension is defined (arbitrarily) as total void volume divided by the total solid–gas interface area, lengths on the order of microns and tens of microns are calculated for the fibrous insulations tested here. Because of this fine microstructure, the local Knudsen number, defined as the gas mean free path over the characteristic pore dimension, can easily reach the slip flow regime ($Kn \sim 0.1-1.0$) at low pressures or high temperatures. For example, the mean free path of air at room temperature and 1 kPa is about 6.5 μm.

To account for increased mass flow because of slip, the effective permeability is expressed as

$$K = K_0[1 + (b/P)] \tag{2}$$

Equation (2) has a form that can be derived from a number of different modeling approaches, e.g., Ref. 5, p. 144, and is sometimes referred to as the Klinkenberg model. K_0 is the material permeability in the limit of continuum flow, and b is a permeability slip parameter that varies with temperature and gas composition. The quantity b/P varies directly with the local Knudsen number. Both K_0 and b are microstructure dependent.

Inserting Eq. (2) into Eq. (1) yields

$$\dot{m} = -\frac{\pi D^2 M}{4\mu RT} K_0(P + b) \frac{dP}{dx} \tag{3}$$

This equation is analogous to that for gas flow in a straight capillary tube with a slip boundary condition[7]; i.e.,

$$\dot{m} = -\frac{\pi d^2 M}{4\mu RT} \frac{d^2}{32} \left(P + \frac{8\mu}{d}\sqrt{\frac{\pi RT}{2M}}\right) \frac{dP}{dx} \tag{4}$$

Comparison of Eqs. (3) and (4) suggests that values of b derived from measurements made at a reference gas composition and temperature can be extended to other gas compositions and temperatures using the relation

$$\frac{b(T, M, \mu)}{b(T_{ref}, M_{ref}, \mu_{ref})} = \frac{\mu}{\mu_{ref}} \sqrt{\frac{T}{T_{ref}} \frac{M_{ref}}{M}} \tag{5}$$

Assuming isothermal conditions, Eq. (3) can be integrated

$$\frac{4\mu\dot{m}RT}{\pi D^2 M} \int_0^L dx = -K_0 \int_{P_1}^{P_2} (P + b)\, dP \tag{6a}$$

or

$$\frac{4\mu\dot{m}RTL}{\pi D^2 M} = K_0 \left[\frac{P_1^2 - P_2^2}{2} + b(P_1 - P_2)\right] \tag{6b}$$

To facilitate the determination of the parameters K_0 and b, Eq. (6b) is rearranged as

$$F = \frac{4\mu\dot{m}RTL}{\pi D^2 M \Delta P} = K_0(P_{av} + b) \tag{7}$$

Because all quantities in F are known or can be measured, K_0 and b can be obtained from a linear least-squares fit of a plot

Table 1 Experimental results for rigid fibrous insulations

	Transverse orientation			In-plane orientation		
Material	ρ, kg/m^3	K_0, 10^{-12} m^2	b, Pa	ρ, kg/m^3	K_0, 10^{-12} m^2	b, Pa
LI-900	127[a]	21.5[b]	3910[c]	136[a]	29.8[b]	3420[c]
	130	19.6	4200	137	29.0	3690
	152	12.0	4940	139	30.2	3400
LI-2200	366	2.90	7640	380	3.59	6950
	370	2.86	7940	386	3.03	7420
	373	2.86	7230	390	3.01	7430
AIM-18	295	4.63	6220	—	—	—
	297	4.32	6850	—	—	—
	306	3.86	7110	—	—	—
	314	4.12	6750	—	—	—
FRCI-12	197	14.8	4200	217	20.1	3740
	206	22.6	3620	217	20.0	3740
	213	14.3	4160	—	—	—
	219	13.3	4440	—	—	—
AETB-12	178	31.5	3120	159	62.9	2390
	182	28.8	3260	184	47.0	2550
	187	23.5	3650	187	33.7	3260
	196	20.3	3590	235	35.4	2850
FiberForm	145	359	703	149	528	784
	149	323	877	152	549	603
	157	82.3	1100	155	514	662
	161	79.1	1150	157	498	725

[a]Density uncertainty: ±1% for all samples. [b]K_0 uncertainty: +11%/−16% for all samples. [c]b uncertainty: +7%/−4% for all samples.

of F vs P_{av}. When evaluating F, the temperature-dependent gas viscosities recommended in Ref. 8 were used.

Experimental Results

Experimental results for the rigid, fibrous insulations are presented and discussed in this section. Room temperature permeability data for air are considered first, then the effects of gas composition and temperature are discussed. A detailed analysis of experimental errors is provided in the next section.

Measured Permeability Parameters

Table 1 presents the results from permeability measurements made on fibrous refractory tile insulations. Figures 3 and 4 show F vs P_{av} plots for LI-2200 and FRCI-12 samples, respectively. These figures are very representative of the type of data and the quality of the curve fit obtained for each of the tile samples listed in Table 1. It should be noted that linear fits to the data are being displayed, but log axes are used for the abscissa to show the spread of the data over multiple orders of magnitude in pressure.

The importance of rarefied flow effects on permeability is demonstrated by the excellent fit between the experimental data and Eq. (7). Figures 3 and 4 also reflect the microstructural anisotropy introduced during the tile manufacturing process. The measured densities of the transverse and the in-plane-oriented specimens compared in Figs. 3 and 4 differ by less than 2%. Nevertheless, the ratio of the in-plane to the transverse values of K_0 is about 5/4 for LI-2200 and 3/2 for FRCI-12. These ratios are a direct consequence of the anisotropic fibrous microstructure that projects a greater solid area on planes normal to the pressing axis than on planes parallel to it. Flow in the transverse direction encounters more obstruction and must take a more tortuous path than flow along the in-plane directions to cover the same macroscopic distance.

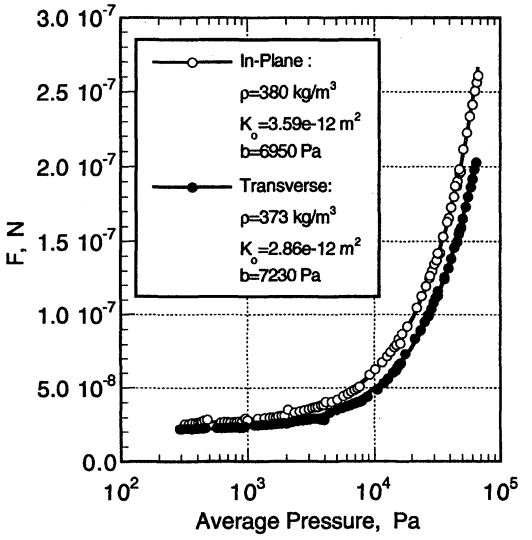

Fig. 3 Experimental data and derived permeability parameters for LI-2200 specimens.

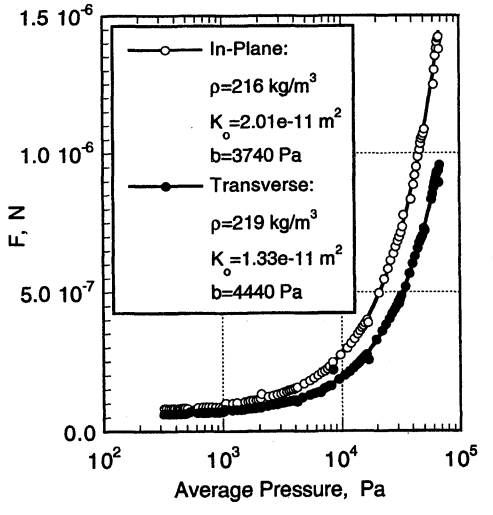

Fig. 4 Experimental data and derived permeability parameters for FRCI-12 specimens.

Figures 5 and 6 show the effect of density variations on the permeability parameters K_0 and b, respectively. The general trends within a given material are that K_0 decreases and b rises with increasing specimen density. This behavior can be related to the microstructural changes that occur as the density increases. A higher density means that more fibers are packed into the same macroscopic volume. The porosity and the characteristic pore size decrease. K_0 falls because the total pore space available for flow is less and the flow path becomes more tortuous. Because the mean distance that a gas molecule can travel before striking a surface is also decreased, rarefied flow effects become important at higher pressures and, consequently, b increases.

In addition to the effect of density variations, Figs. 5 and 6 show the influence of insulation composition on the permeability parameters. LI-900, LI-2200, and AIM-18 are silica fiber insulations, whereas FRCI-12 also contains Nextel® fibers, and AETB-12 also contains Nextel and alumina fibers. The silica and alumina fibers are blown fibers and have fiber diameter distributions of several microns centered at about 2 and 3 μm, respectively. The Nextel fibers are drawn fibers with diameters close to 8 μm. As expected from density considerations alone, the average values of K_0 decrease and the average values of b increase going from LI-900 to AIM-18 to LI-2200. Note, however, that FRCI-12 and AETB-12 have nominal densities 33% greater than LI-900, yet their values of K_0 are comparable to or greater than those of LI-900, and their values of b are com-

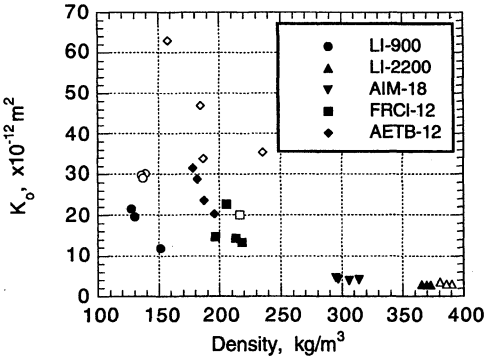

Fig. 5 Variation of K_0 with sample density. Solid symbols indicate the transverse direction and open symbols the in-plane direction.

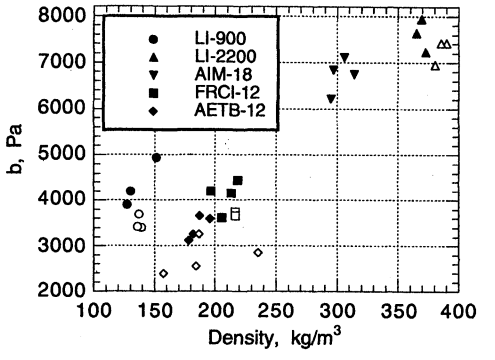

Fig. 6 Variation of b with sample density. Solid symbols indicate the transverse direction and open symbols the in-plane direction.

parable to or less than those of LI-900. The reason for this is the incorporation of the larger Nextel fibers into the microstructure. Though FRCI-12 and AETB-12 are denser than LI-900 on a macroscopic scale, the microstructure is actually coarser because mass is concentrated into larger fibers (on average). The addition of Nextel also promotes sintering between silica fibers because of the release of boron during firing, and this process tends to consume the smallest silica fibers. As a result, the flow path is less tortuous and the mean path between gas-surface collisions is longer than it would be in an all-silica fiber tile of the same density. The effect of fiber size on permeability is illustrated most dramatically when comparing the results for FiberForm to those for the ceramic fiber tiles (see Table 1). The carbon fibers that make up FiberForm have diameters of about 15 μm, and as a consequence K_0 can be 15 times larger and b about 5 times smaller than for an LI-900 specimen of comparable density.

Gas and Temperature Dependence

The effect of gas composition on the permeability parameters K_0 and b was tested using helium as the flow gas. The experimental data obtained with air and helium on the same in-plane oriented LI-2200 specimen are shown in Fig. 7. The permeability parameters derived from the air data are K_0 = 3.03e-12 m^2 and b = 7420 Pa, and those derived from the helium data are K_0 = 2.96e-12 m^2 and b = 21,800 Pa. The

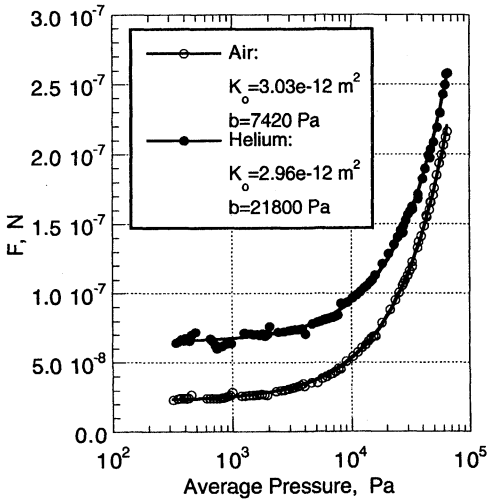

Fig. 7 Experimental data and derived permeability parameters for an in-plane oriented LI-2200 specimen using air and helium as test gases.

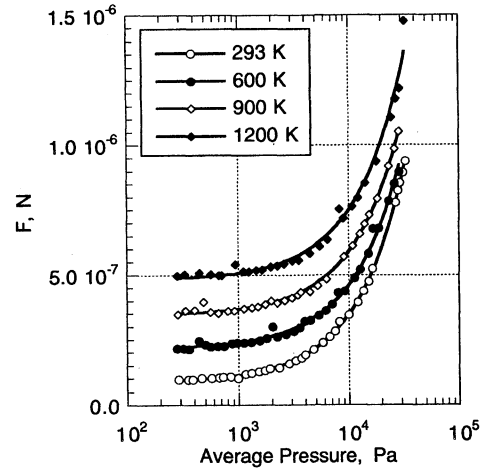

Fig. 8 Experimental data for a transversely oriented AETB-12 specimen taken at four different temperatures.

Table 2 Experimental results for temperature-dependent experiment

T, K	K_0, 10^{-12} m^2	b, Pa	$K_0/K_{0,293}$	$(b/\mu\sqrt{T})/(b/\mu\sqrt{T})_{293}$
293[a]	25.9[b]	3,370[c]	1.00	1.00
600	24.5	8,780	0.95	1.09
900	24.5	14,000	0.95	1.09
1200	26.8	18,000	1.02	1.02

[a]Temperature uncertainty: ±2% for all cases. [b]K_0 uncertainty: +11%/−16% for all cases. [c]b uncertainty: +7%/−4% for all cases.

values of K_0 are within 3% of each other and are identical to within the experimental uncertainties of the measurement. This result supports the premise that K_0 is an intrinsic material property independent of the flow environment. The scaling relation of Eq. (5) can be used to predict the value of b in helium based upon the measured value of b in air. Assuming a constant temperature of 290 K for both experiments, the viscosities of air and helium are 18.05e-6 and 19.42e-6 N-s/m^2, respectively.[8] The molar mass of air is 0.02897 kg/mol and that of He is 0.00400 kg/mol. With these values, Eq. (5) predicts a value of 21,490 Pa for He, which is within 2% of the experimentally determined value.

Figure 8 shows experimental data obtained on a transversely oriented AETB-12 specimen that was tested at four different temperatures (293, 600, 900, and 1200 K), using the quartz test section and tube furnace described in the experiment section. Because the thermal expansion coefficient of AETB-12 is several times larger than that of quartz, a tight fit between sample and test section was assured by doing successive experiments in order of increasing temperature. The first three columns of Table 2 list the test temperatures and values of the permeability parameters extracted from the data of Fig. 8. The fourth and fifth columns give the values of K_0 and $b/\mu\sqrt{T}$ normalized by their values at 293 K. These ratios are within 5 and 10% of unity for K_0 and $b/\mu\sqrt{T}$, respectively, and can be considered constant and independent of temperature, within the experimental errors of the measurement. Thus, the continuum permeability is demonstrated to be independent of temperature as postulated, and the temperature dependence of b, as embodied in Eq. (5), is confirmed.

Experimental Error

There are several potential sources of error that contribute to the uncertainties in K_0 and b. The most obvious of these is the possibility of gas leakage past the test specimen. The experimental signatures of a "leaky" specimen are examined in detail in the following subsection. A complete uncertainty analysis is presented thereafter.

Parallel Flow Paths

If there is any significant gas leakage around the test specimen or if internal flow channels of significantly different flow resistance exist in the sample microstructure, the net gas flow is a sum of parallel flows. Deviations from the form of Eq. (7) are then expected because the flow resistance of each path and the transition points between various flow regimes (as indicated by the local Reynolds and Knudsen numbers) will differ. The following experiment was conducted to understand the effects of gas leakage on experimental flow data and the derived permeability parameters. An in-plane oriented LI-2200 specimen was tested to obtain baseline flow data. A ~350-μm-diam hole was then drilled through the length of this sample (while still in the holder), and the sample was retested. The resulting data are displayed in Fig. 9. It is obvious that the presence of the hole causes the data to depart from the theoretical model. Because the hole is continuous and of a diameter at least an order of magnitude greater than the characteristic pore dimension in LI-2200, more mass flow is expected for the same pressure gradient. The experimental data indicate that the flow contribution of the hole is more prominent at higher

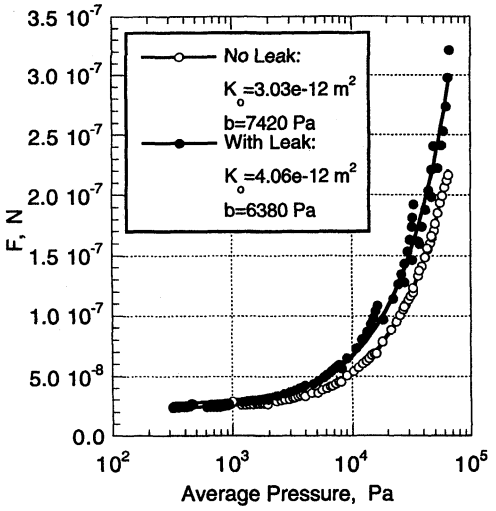

Fig. 9 Experimental data and derived permeability parameters for an in-plane oriented LI-2200 specimen with and without a 350-μm-diam leak.

pressures, and the data deviate from a smooth monotonic curve in this pressure regime. This observation can be understood in a qualitative way by taking the ratio of Eqs. (4) and (3) to model the ratio of the hole and porous plug flow rates:

$$\frac{\dot{m}_H}{\dot{m}_P} = \frac{\frac{d^4}{32}\left(P + \frac{8\mu}{d}\sqrt{\frac{\pi RT}{2M}}\right)}{D^2 K_0 (P + b)} \tag{8}$$

With the appropriate numerical values this equation becomes

$$\frac{\dot{m}_H}{\dot{m}_P} \cong 0.48\left(\frac{P + 150}{P + 7420}\right) \tag{9}$$

From this relation it is evident that the flow contributions of the hole are negligible at low pressures but become very prominent as the pressure is raised, in full agreement with experiment.

The departure of the data from the theoretical relation of Eq. (3) may be related to the fact that at higher pressures a larger fraction of the flow is passing through the hole, and this flow may be in various different flow regimes that are not modeled well by Darcy's law. According to Ref. 7, the Darcy flow regime lies below a Reynolds numbers of about 1, the inertial flow regime within the range 1 to 150, the unsteady laminar regime between 150 and 300, and the turbulent regime above 300. The Reynolds number based upon the hole diameter can be expressed as

$$Re_H \equiv \frac{d\dot{m}_H}{\mu \pi d^2/4} \cong 2 \times 10^8 \dot{m}_T \left(\frac{0.48P + 72}{1.48P + 7492}\right) \tag{10}$$

Experimentally, the total mass flow rates ranged from about 3.0e-8 to 8.e-5 kg/s, and the average pressure from about 470 to 67,000 Pa. These values produce a Reynolds number range that varies from about 0.2 at low pressure to about 480 at high pressure; therefore, clearly the presence of the hole can cause deviation from Darcy's law.

Error Analysis

The effect of gas leakage by a test specimen would be to artificially raise the value of K_0 and lower the value of b. As stated previously, the design of the experiment and the techniques used are believed sufficient to prevent this possibility. Any residual gas leakage must have been very small, and because of the highly porous nature of fibrous refractory insulations, it was most likely negligible compared to the gas flow through the test specimen. Note that in the extreme case presented in the previous subsection, where a ~350-μm-diam hole was created in an LI-2200 sample, the value of K_0 changed only about +35% and the value of b changed −15%. In a less dense sample a leak of this size would have resulted in even smaller changes. If residual leaks are idealized as capillaries, it is easy to see from Eq. (8) that the leak flow contribution decreases rapidly (at least as d^3) with decreasing diameter. Any residual leaks would have effective diameters at least an order of magnitude smaller than in the LI-2200 sample (otherwise they would result in discontinuous F vs P_{av} curves and be easily detected in the plotted data), and so the potential error introduced into K_0 and b becomes extremely small. To be conservative, an uncertainty of +0/−5% and +2/−0% is assigned to K_0 and b, respectively, based solely on the possibility of some residual gas leakage. Permeabilities are strictly defined only for homogeneous media. Samples with visible microstructural defects—such as pits or voids in the surfaces—were not tested. It is possible that some specimens contained internal defects of this type; however, posttest serial sectioning of several different specimens did not reveal any. The influence of such defects on measured permeabilty parameters cannot be isolated and they are effectively considered part of the sample microstructure if they occur.

Because K_0 and b are obtained from a fit of F vs P_{av}, errors in the latter two quantities can also contribute uncertainties. The uncertainty in P_{av} is estimated at about ±2%, and numerical tests indicate that comparable uncertainties are introduced into K_0 and b. Assuming independent uncertainties in the individual quantities, the rms relative uncertainty in F can be expressed as

$$\omega_F = \sqrt{\omega_\mu^2 + \omega_{\dot{m}}^2 + \omega_R^2 + \omega_T^2 + \omega_L^2 + 4\omega_D^2 + \omega_M^2 + \omega_{\Delta P}^2} \tag{11}$$

where $\omega_F = \delta F/F$, etc. Of the individual uncertainties, those associated with R, M, L, and D are ±0.1% or less and can be considered negligible. The uncertainties in T and ΔP are estimated at about ±1%, and those in μ and $\dot{m}$ at about ±5%. This leads to an estimate of about ±8% for ω_F. Because of the form of Eq. (7), this uncertainty translates directly to K_0 but leaves b unaffected. A final source of uncertainty is the sensitivity of the fitting process to fluctuations in the data around the theoretical curve. It is found that b is more sensitive to outlying data points than K_0. Based on numerical tests, reasonable estimates of the uncertainties introduced by data fluctuations are ±1 and ±3%, for K_0 and b, respectively. Adding up these various uncertainties gives an overall estimate of the uncertainty associated with each permeability parameter; viz., +11/−16% for and +7/−4% for b. These uncertianties are listed in the footnotes to Tables 1 and 2.

Computational Example

The availability of gas permeability data for rigid fibrous insulations enables the computational analysis of various flow problems relevant to TPS systems. The venting of a space probe is an example where a rigid porous refractory insulation may find a useful application. The maximum pressure differential between the inside and outside of the probe must stay below a prescribed limit, typically less than 10 kPa. Traditionally, vents made of a fine metallic mesh are used for this purpose. However, if a probe is to make an atmospheric entry from space, these vents must be positioned in low heat flux areas to avoid overheating the vent. As the atmospheric entry heating environment becomes more extreme, e.g., sample return missions, this approach has obvious limitations, and it becomes more desirable to use a porous ceramic vent. Preliminary heating and flow tests, as well as numerical analyses,

indicate that a vent thickness in the range of 2–5 mm is appropriate for such an application.

The vent must maintain the pressure differential within desired bounds during both launch and atmospheric entry. For the launch phase, a spacecraft typically resides within a cargo bay. The internal environment can be considered isothermal but with varying (decreasing) external pressure. Assuming negligible gas storage within the vent and constant internal temperature, the internal pressure of the gas volume V that is vented through a porous material can be described by the nonlinear first-order differential equation

$$\frac{dP_{int}}{dt} = -\frac{AK_0}{VL\mu}\left[\frac{P_{int}^2 - P_{ext}^2}{2} + b(P_{int} - P_{ext})\right] \quad (12)$$

The cargo-bay pressure, P_{ext}, is a prescribed function of time. Equation (12) can be integrated in a straightforward manner using a fifth-order Runga–Kutta integration routine.[9]

As a numerical example, consider a probe fit with an in-plane oriented AETB-12 vent that is launched on a Delta II rocket. The values of K_0 and b were taken as 33.7×10^{-12} m^2 and 3260 Pa, respectively. A typical transient payload compartment pressure during launch was obtained from Ref. 10. Figure 10 shows the predicted pressure differentials experienced by the probe, for several values of the parameter combination A/VL. Depending on the volume to be vented and the maximum pressure differential allowed, the required vent dimensions can be easily determined.

For the atmospheric entry phase, both the external pressure and the aerothermal heat flux must be taken into account. The thin vent is treated as a lumped mass, gas storage inside the vent is neglected, the gas is assumed to enter the spacecraft at the vent temperature, and the gas equilibrates inside the spacecraft. Four differential equations are solved for the vent temperature T_P, the internal gas temperature $T_{g,int}$, an effective internal solid temperature $T_{s,int}$, and the mass of gas inside the spacecraft m (where $P_{int}MV = mRT_{g,int}$):

$$\frac{dh_p}{dt} = \frac{q_{ext} - \sigma\varepsilon_p T_p^4}{L\rho_p} \quad (13a)$$

$$\frac{du_{g,int}}{dt} = \max\left[0, \frac{\dot{m}}{m}(h_g|_{T_p} - u_{g,int})\right] - \frac{HA'(T_{g,int} - T_{s,int})}{m} \quad (13b)$$

$$\frac{dm}{dt} = \frac{AMK_0}{\mu RLT_p}\left[\frac{P_{ext}^2 - P_{int}^2}{2} + b(P_{ext} - P_{int})\right] \quad (13c)$$

$$\frac{dT_{s,int}}{dt} = \frac{HA'(T_{g,int} - T_{s,int})}{(mC_p)_{s,int}} \quad (13d)$$

In the preceding equations H and A' are an effective heat transfer coefficient and area, respectively, for heat exchange between the vented gas and the solid mass $m_{s,int}$ inside the spacecraft. The quantities $(mC_p)_{s,int}$ and HA'/m are sufficiently large to prevent interior temperatures from becoming too high. The scaling relation of Eq. (5) is used for b in Eq. (13c). The temperature variation of the gas and solid heat capacities is taken into account in evaluating the internal energy and enthalpy terms in Eqs. (13a–d).

Pressure and heating environments (P_{ext} and q_{ext}) have been computed for the aft heatshield of the Stardust sample-return capsule.[11] On the aft conical section, the peak heating and total heat load were predicted to be less than 8.5 W/cm^2 and 270 J/cm^2, respectively. With a single-use temperature limit of over 1860 K, an AETB-12 vent can withstand more than double this heating environment. Thus, the primary concern is sizing the vent area and thickness to maintain a pressure differential below the design value. Equations (13a–13d) were solved using the Runga–Kutta routine mentioned previously with an initial condition of 200 K and a range of vent thicknesses and interior heat transfer parameters. The maximum pressure differential increases as the internal heat transfer (gas to solid) becomes more effective, because P_{int} is proportional to $T_{g,int}$ through the ideal gas law.

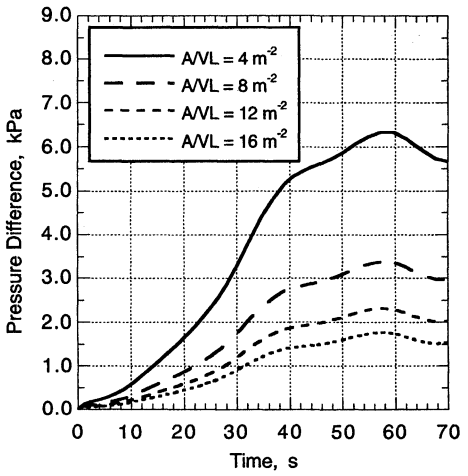

Fig. 10 Transient pressure differential for a spacecraft, with AETB-12 in-plane oriented vents, subject to a typical payload compartment pressure environment during launch of a Delta II rocket.

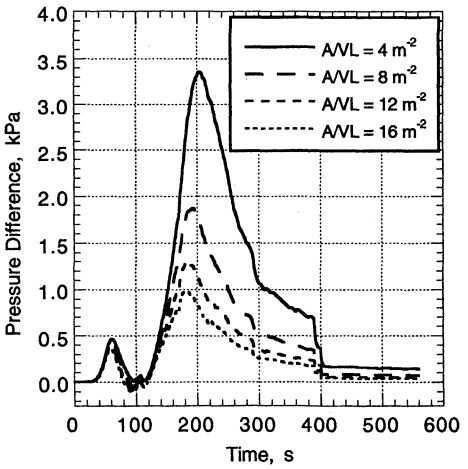

Fig. 11 Transient pressure differential for a spacecraft, with 2-mm-thick AETB-12 in-plane oriented vents, subject to the entry pressure and heating environment for the afterbody of the Stardust sample-return capsule.

Figure 11 shows the predicted pressure differential histories for several values of the A/VL, for a vent thickness of 2 mm and for the worst case of an isothermal cold interior. The pressure differential changes sign, because the prescribed external pressure history has local maxima and minima during the deceleration of the probe.[11] Comparison of Figs. 10 and 11 reveals that for the same value of A/VL the maximum pressure differential is higher during launch than during entry owing to the faster time scale for pressure variations in the former case.

Summary

An experimental procedure was developed for measuring the gas permeability of rigid fibrous tile insulations. Permeability data were documented for a variety of such insulations including the LI, AIM, FRCI, and AETB families, as well as FiberForm. The permeability is, in general, orthotropic; therefore, measurements were obtained for both in-plane and transverse sample orientations. For all materials except FiberForm, continuum permeabilities range from 3 to 63 $\times 10^{-12}$ m^2;

FiberForm has a significantly higher permeability on the order of 80–550 $\times$ 10^{-12} m^2.

The dependence of permeability on gas pressure and material density were presented. Rarefied-flow effects were shown to be significant. At room temperature the permeability slip parameter for air was found to range from 603 to 7940 Pa. The postulated dependence of the slip parameter on gas composition and temperature was validated by experiment. A representative computation was presented of flow through a rigid fibrous insulation in application as a spacecraft vent.

Acknowledgments

This work was partially supported by NASA Contract NAS2-14031 to Eloret Corporation. The authors acknowledge the diligent work of Jamie Lascon, Lesanne Etienne, Jerry Ridge, and Micheal Cox in helping to accumulate the experimental flow data presented herein. Janine Thornton from Lockheed Martin provided pressure histories that were used to size vents for the Stardust probe.

References

[1]Marschall, J., and Milos, F. S., "Gas Permeability of Rigid Fibrous Refractory Insulations," AIAA Paper 97-2479, June 1997.

[2]Leiser, D. B., Smith, M., and Stewart, D. A., "Options for Improving Rigidized Ceramic Heatshields," *Ceramic Engineering and Science Proceedings*, Vol. 6, No. 7–8, 1985, pp. 757–768.

[3]Stewart, D. A., and Leiser, D. B., "Characterization of the Thermal Conductivity for Fibrous Refractory Insulations," *Ceramic Engineering and Science Proceedings*, Vol. 6, No. 7–8, 1985, pp. 769–792.

[4]Banas, R. P., Creedon, J. F., and Cunnington, G. R., Jr., "Thermophysical and Mechanical Properties of the HTP Family of Rigid Ceramic Insulation Materials," AIAA Paper 85-1055, June 1985.

[5]Scheidegger, A. E., *The Physics of Flow Through Porous Media*, Macmillan, New York, 1957.

[6]Incropera, F. R., and DeWitt, D. P., *Fundamentals of Heat Transfer*, Wiley, New York, 1981, Chap. 8.

[7]Kaviany, M., *Principles of Heat Transfer in Porous Media*, 2nd ed., Springer–Verlag, New York, 1995.

[8]Touloukian, Y. S., Saxena, S. C., and Hestermans, P., "Thermophysical Properties of Matter," *Viscosity*, Vol. 11, IFI/Plenum, New York, 1975.

[9]Press, W. H., Teukolsky, S., A., Vetterling, W. T., and Flannery, B. P., *Numerical Recipes in FORTRAN*, 2nd ed., Cambridge Univ. Press, Cambridge, England, UK, 1992, Chap. 16.

[10]Anon., "Delta II Payload Planners Guide," McDonnell Douglas Aerospace, MDC H3224C, Huntington Beach, CA, Oct. 1993.

[11]Olynick, D. R., Chen, Y.-K., and Tauber, M. E., "Wake Flow Calculations with Ablation for the Stardust Sample Return Capsule," Paper AIAA 97-2477, June 1997.